

Bioactive nanoparticles for boosting tumor immunotherapy via Ca²⁺ interference mediate TME reprogramming and PD-L1 depletion

Jinjin Shi (✉ shijinyxy@zzu.edu.cn)

Zhengzhou University <https://orcid.org/0000-0003-1531-7265>

Jingyi An

Zhengzhou University

Kaixiang Zhang

Zhengzhou University

Mengyuan Liu

Zhengzhou University

Ling Zhao

Zhengzhou University

Wenxin Lu

Zhengzhou University

Junjie Liu

Zhengzhou University

Sixuan Wu

Zhengzhou University

Zhenzhong Zhang

Zhengzhou University

Article

Keywords: tumor immunotherapy, Ca²⁺ interference, tumor immunosuppressive microenvironment, PD-L1 depletion, DNase

Posted Date: March 16th, 2021

DOI: <https://doi.org/10.21203/rs.3.rs-313336/v1>

License:   This work is licensed under a Creative Commons Attribution 4.0 International License.

[Read Full License](#)

Abstract

The efficacy of antitumor immunotherapy is often limited by the highly tumor immunosuppressive microenvironment (TME). Here, a previously unknown strategy is proposed to synergize the “Ca²⁺ interference” mediate TME reprogramming and Ca²⁺-activating PD-L1 depletion for immunotherapy. We discovered that calcium containing nanoparticles could induce significant “Ca²⁺ interference” effect and simultaneously resetting tumor-associated macrophages toward M1 phenotype and promoting in situ antigen release. Making them as powerful immunostimulants for TME reprogramming without notable toxicity. Meanwhile, we designed a circular aptamer-DNAzyme conjugate (cAD) with tumor-targeting ability and its catalytic shear activity can be specifically activated by Ca²⁺, which reduces potential autoimmune disorders of PD-L1 antibody. By simple integrating the ultra-high pH sensitive calcium peroxide nanoparticles with cAD into one nanosystem, we demonstrate the nanosystem not only arrests primary tumor progression, but also prevents lung metastasis. In addition, it offers a long-term immunological memory function, which can protect against tumor rechallenge. Therefore, this work provided an alternative strategy for boosting tumor immunotherapy.

Introduction

Immunotherapy is rapidly rising as a promising strategy for the treatment of tumor^{1, 2}. Nevertheless, its efficiency is limited by immunosuppressive tumor microenvironment (TME) and poor immunogenicity of tumor cells^{3, 4}. Although multiple factors in TME contribute to the failure of immunotherapy, one dominant reason is the recruitment of suppressive immune cells, such as tumor-associated macrophages (TAMs), regulatory T cells (Tregs) and cancer-associated fibroblast (CAFs) etc. al, which always lead to immune evasion by limiting T cell infiltration and functions⁵. Besides, tumor cells usually escape the immune surveillance via concealing neoplasma antigen (poor immunogenicity)⁶. Therefore, selectively reprogramming immunosuppressive TME and immunogenicity is recognized as an extremely promising strategy for immunotherapy. One relatively efficient approach is to develop nanomedicine to deliver immunomodulatory and therapeutic drugs to tumors^{7, 8}. Despite the advances in nano immunotherapy systems, compatibility of loaded drugs including the types and loading amount need to be precisely adjusted. Furthermore, distinct targets of loaded drugs require harsh differentiated drug release between immune and tumor cells, thus putting forward an extremely formidable task for the design and fabrication of nano carriers, which introduces more uncertainty for their further clinical application.

There is growing evidence that metal ions are critically implicated in regulating both innate and adaptive immune response, one possible way to overcome the above challenges is “metal ions interference”. Particular Ca²⁺, as a second messenger, is a pivotal player in immune cell activation and phenotypic transformation⁹. For example, with the increase of cytosolic Ca²⁺, the central transcriptional regulators for lymphocyte and macrophage activation include NFAT, NF-κB, the kinase Jnk and calmodulin-dependent kinase are highly activated¹⁰⁻¹². Furthermore, the effector function of NK, macrophages and CTL, as well as their proliferation and cytotoxicity to tumor cells largely depend on cytosolic Ca²⁺.

Interestingly, we and other groups also found that Ca^{2+} overloading in tumor cells could lead to the enhanced release of multiple damage-associated molecular patterns (DAMPs), such as up regulation of “eat me” signal calreticulin (CRT), release high mobility group protein 1 (HMGB1), which significantly improved the immunogenicity of tumor cells^{13, 14}. Given the multiple immunostimulatory effect, we propose that calcium containing nanoparticles may serve as attractive materials for developing tumor immunomodulation platform. Besides, the activation of adaptive immune response often leads to the upregulation of PD-L1 expression in tumors, which needs further immune checkpoint blockade¹⁵. But the general application of PD-L1 antibody often leads to significant autoimmune disorders. Therefore, it’s also highly desired to locally suppress the expression of PD-L1 on tumor cells.

Herein, we propose applying dual-targeted immunomodulatory strategy using “ Ca^{2+} interference” to stimulate antitumor immune response and activatable gene silencing in tumor cells to deplete PD-L1. Notably, TAMs, as the major tumor-infiltrating immune cell population (over 50% of the cells in tumor), are believed to play critical roles in immunosuppressive TME. Moreover, as a professional phagocyte, TAMs are also believed as the main reservoir of nanoparticles in tumor¹⁶. As expected, we demonstrated that nano enable “ Ca^{2+} interference” conferred strong “re-educating” effect on TAMs, and surprisingly, stimulated both innate and adaptive immune responses in tumors.

To achieve local PD-L1 suppression, we designed a circular aptamer-DNAzyme conjugate (cAD) loaded in the designed calcium nanoparticle, which can be specifically released in tumor site for efficiently PD-L1 gene silencing. Comparing with traditional siRNA-based gene silencing strategy, cAD holds high stability *in vivo* and can be spontaneously uptaken by tumor cells, due to the circular structure and functional aptamer sequence¹⁷. Besides, DNAzyme are catalytic nucleic acids that can mimic the function of endonucleases for cleavage of specific mRNA with multiple turnovers, which may be more effective for PD-L1 gene silencing on a per molecule basis^{18, 19}. However, DNAzymes always need sufficient ion cofactor supply for activation, which just can be solved by our “ Ca^{2+} interference” strategy^{20, 21}. Since Ca^{2+} release was also specific in tumor site in response to the relatively low pH, this integrated system showed high tumor specificity for local PD-L1 suppression.

In this study, we designed nanoparticles that contain a calcium core, cAD and a hydrophilic shell (SDS-PEG2000) for efficient immunotherapy. This immunotherapeutic nanoplatform exhibits multifunctional characteristics, including (i) improve stability in blood circulation, thus leading to the enhanced tumor accumulation of NPs²²; (ii) super sensitive pH response, leading to the site-specific release of cAD in TME, cAD target to tumor cells for Ca^{2+} -activating PD-L1 depleting; (iii) calcium cores ingested by TAMs achieve efficient “ Ca^{2+} interference”, leading to the dephosphorylation of p38, activation of NF- κ B to promote nuclear translocation, and release of NLRP3 inflammasomes, obtaining a synergetic activation of both innate and acquired immune responses^{23, 24}; (iv) “ Ca^{2+} interference” in tumor cells that can activate calmodulin and serve as an inducer to the release of multiple tumor antigens (CRT, HMGB1), further promoting tumor cell immunogenicity. We demonstrated that the simple nanoplatform exhibited

potent efficacies as a treatment against both primary and metastatic tumors without obvious side effects.

Results

CaNP resets tumor-associated M2 macrophages to M1 phenotype

Calcium nanocarriers (calcium peroxide (CaO_2), calcium phosphate (Cap) and honeycomb calcium carbonate (HOCN)) were synthesized according to the methods previously reported²⁵⁻²⁷. Monodispersed nanoparticles with sizes of ~150 nm, ~50 nm and ~200 nm were obtained, respectively (Fig.1A). CaO_2 nanoparticle (CaNP) was selected for realizing “ Ca^{2+} interference” due to its excellent acid sensitivity, most efficient Ca^{2+} release performance and distinctive positive electrical property, which facilitates subsequent cAD loading (Fig.1B, C and Supplementary Fig.1A, B). As a second messenger, Ca^{2+} is believed to play critical roles in immune cell activation and phenotypic transformation. Here, we asked whether CaNP would induce the polarization of TAMs. Mice bone-marrow-derived macrophage cells (BMDMs) were harvested and treated following the operation procedure in Fig.1D. With prolonged incubation time, a gradual increase of Ca^{2+} levels in BMDM-M2 was observed (Supplementary Fig. 2A, B), suggesting the efficient endocytosis of BMDM-M2, and CaNP showed a neglectable cytotoxicity on BMDM-M2 (Supplementary Fig. 2C). More important, we found that CaNP treatment group visually indicated a significant increased in M1-phenotype (CD80^+) and a decreased in M2-phenotype (CD206^+) compared with Cap NP and H_2O_2 treatment group (Fig.1E), indicating that CaNP had a synergetic enhancement on “re-educating” TAMs. The decrease in immunosuppressive factor interleukin-10 (IL-10) and the increase in immune activating factor interleukin 12p70 (IL-12p70) secretion of CaNP treatment group further confirmed the successful phenotypic regulation (Fig.1F).

With the change of macrophage phenotype, its phagocytosis to B16 cells also showed an obvious enhancement in vitro (Fig.1G). At the same time, two main chemokines including CXCL9 and interferon- γ (IFN- γ) were observed a significant increase in CaNP treatment BMDM-M2 (Fig.1H). Specifically, CXCL9 is considered to be an important chemokine for the recruitment of CD8^+ T cells into tumors. Therefore, we used transwell to investigate the recruitment effect of CaNP treated BMDM-M2 on CD8^+ T cells in vitro (Fig.1I, left). As expected, CaNP treated group induced obviously CD8^+ T cells infiltration in the below room, almost as the positive control (LPS/ IFN- γ treated group) (Fig.1I, right). What’s more interesting, besides the recruitment of CD8^+ T cells, the proliferation of CD8^+ T cells was also promoted by CaNP treatment. In brief, 5,6- carboxyfluorescein diacetate succinimidyl ester (CFSE) labeled CD8^+ T cells were co-cultured with pretreated BMDM-M2, after CaNP treatment, the number of CD8^+ T cells increased from ~10.7% to ~30.1% and induced more obvious cell proliferation than other groups (Fig.1J). These data demonstrate that CaNP could efficiently regulate the phenotype and function of TAMs via “ Ca^{2+} interference”, which is essential for stimulating antitumor immune response.

We discovered that CaNP could induce significant “Ca²⁺ interference” effect and have a synergetic enhancement on resetting TAMs toward M1 phenotype, which was also confirmed by the highest expression of iNOS in CaNP group compared with CaP and H₂O₂ treatment (Fig. 2A and Supplementary Fig.3A left). And then, we investigated the underlying molecular mechanism. According to the previous studies, mitogen-activated protein kinase (MAPK) and nuclear factor-κB (NF-κB) signal molecules are highly activated in M1 macrophages, and they also play the key role in regulation of proinflammatory factors, such as IL-12p70. Therefore, a mainly MAPK members (p38) was firstly analyzed. What excited us is that only calcium containing nanoparticle (CaNP and CaP) induced the phosphorylation of p38 in BMDM-M2 macrophages (Fig. 2A and Supplementary Fig.3A right). To further conform this, we used cyclosporin A (CsA), a Ca²⁺ signaling inhibitor to pre-treatment with BMDM-M2, the effect of CaNP on p38 phosphorylation was significantly blocked (Fig. 2B and Supplementary Fig. 3B), suggesting that “Ca²⁺ interference” promotes the development of M1 phenotype through p38 molecule. Secondly, we tested the influence of “Ca²⁺ interference” on NF-κB by examining its nuclear translocation. Compared with the control group, we found CaNP treatment resulted in the colocalization of NF-κB with nucleus in BMDM-M2 macrophages, while the nuclear translocation could be significantly blocked by CsA (Fig. 2C). The above results illustrated that both the activation of MAPK (phosphorylation of p38) and nuclear translocation of NF-κB are involved for “Ca²⁺ interference”-mediated TAMs resetting. Besides the phenotypic changes of TAMs, our previous research showed that “Ca²⁺ interference” could increase the reactive oxygen species (ROS) level of mitochondrion⁽²⁵⁾, and ROS-mediated mitochondrial dysfunction triggers the NLRP3-inflammasome pathway for activating the innate immune response of macrophages²⁸. According to this, IL-1β secretion of BMDM-M2 macrophages with different treatments was investigated. As expected, a significant increase of IL-1β secretion was observed in BMDM-M2 treated with CaNP, while showing an obvious blockade after catalase (CAT) treatment (Fig. 2D), indicating that “Ca²⁺ interference”-mediated IL-1β secretion is ROS depended. Active caspase-1 converts pro-IL-1β to mature IL-1β that stimulates inflammation²⁹. Therefore, the increase of caspase-1 expression in CaNP-treated BMDM-M2 further confirmed the result of IL-1β secretion (Fig. 2E), which can stimulate the strong innate immune response of macrophages.

For further investigation of the molecular mechanisms involved in the CaNP-induced macrophage polarization. We obtained the differentially expressed genes in CaNP+CAT treated BMDM-M2 cells by transcriptome analysis. Several genes related to inflammation suppression phenotype were significantly downregulated (*i.e.* Arg1, CD163, Il4ra, Il13ra2), while upregulating the expression of inflammation-related genes (*i.e.* Tnfsf15, Tlr12, Pik3cb) (Fig. 1G and Supplementary Fig. 3C) after CaNP + CAT treatment. Kyoto Encyclopedia of Genes and Genomes (KEGG) pathway analysis revealed the important role of inflammation-related pathway such as NF-κB signaling pathway, chemokine signaling pathway and cytokine–cytokine receptor interaction in the CaNP+CAT-treated group (Fig. 2H). Given those results, one possible explanation might be attributed to the multiple mechanisms of Ca²⁺ induced macrophage polarization.

cAD efficiently depletes PD-L1 in tumor cells

The design, composite and preparation diagram of cAD is shown in Fig. 3A. In brief, phosphorylated cell-specific aptamer (Sgc8)³⁰ and Ca²⁺-specific DNAzyme named EtNa³¹ were hybridized with complementary sequences, and then two gaps were sealed with T4 DNA ligase (See Supplementary table 1 for specific sequence information). The results of agarose gel electrophoresis illustrated the successful synthesis of CAD (Fig. 3B). We then investigated whether cyclization enhances the stability of EtNa in biological medium. As shown in Fig. 3C, D, Sgc8 and EtNa were significantly degraded after incubation in exonuclease I or DMEM-10% fetal bovine serum, while the integrity of each conjugate was still evident for CAD under the same conditions. (Fig. 3D). Next, we examined whether cyclization affected the performance of EtNa and Sgc8. Fig. 3E showed that cAD had an enzyme cleavage effect, and the cleavage efficiency is Ca²⁺ concentration-dependent. Furthermore, we performed fluorescent detection to investigate the cleavage efficiency of cAD (Fig. 3F), and both the enzyme cleavage effect of EtNa and cAD showed a strong Ca²⁺ activated property. Interestingly, cAD displayed a significant increase in the cleavage efficiency than that of EtNa (Fig. 3G), indicating that the enhanced stability of cAD improves the affinity with the substrate. The cyclization of Sgc8 and EtNa to obtain cAD not only brings the enhanced stability and improved cleavage efficiency, but also makes cAD have a high tumor specificity for tumor cell specific PD-L1 suppression. Therefore, the tumor cell specific reorganization and targeting ability of cAD was confirmed via flow cytometry and confocal microscope (Fig. 3H).

DNAzymes need sufficient ion cofactor supply for activation, which just can be solved by our “Ca²⁺ interference” strategy. In turn, Ca²⁺ interference also can active cAD for PD-L1 depleting. A significant Ca²⁺ interference effect was observed in B16 tumor cells after treated with CaNP, and the level of Ca²⁺ in tumor cells increased with the prolongation time of CaNP incubation (Fig. 3I). Interestingly, we also observed that the lysosomal escape of cAD was significantly enhanced with the addition of CaNP (Supplementary Fig.4), which is advantageous to the PD-L1 mRNA cleavage. Accordingly, the expression level of PD-L1 in B16 tumor cells treated with CaNP+cAD was significantly reduced compared with those treated with CaNP or cAD alone (Fig. 3J). This phenomenon was also confirmed by qRT-PCR (Fig. 3K, primer sequences are shown in Supplementary table 2). Notably, with Ca²⁺ interference effect induced by CaNP, the PD-L1 level and mRNA level of cAD significantly reduced, further indicating the Ca²⁺ activating property of cAD. Furthermore, our previous studies have shown that the increase of intracellular Ca²⁺ promotes the release of multiple tumor antigens, such as the exposure of CRT and the release of HMGB1 in CT26 cells²⁷, and this effect of Ca²⁺ interference was also confirmed in B16 tumor cell for further improving the tumor cell immunogenicity (Fig. 3L, M). These results indicated that cAD combined with CaNP can not only improve the tumor cell immunogenicity, which is conducive to the occurrence of anti-tumor immunity, but also reduce the expression of PD-L1 in tumor cells and restore the function of T cells.

CaNP@cAD-PEG effectively inhibites tumor growth

After evaluating the performance of CaNP on phenotypic transformation of TAMs and cAD on tumor cell specific PD-L1 depleting, respectively, we aimed to combine the two into one nanoparticle for efficient delivery in vivo. Firstly, cAD was loaded onto the surface of CaNP due to its positive electrical property, and the optimal loading ratio of CaNP to cAD is 10:1 (V: V, CaNP: 5 mg/mL, cAD: 10 μ M, Supplementary Fig.5A). After cAD loading, a hydrophilic shell (DSPE-PEG2000) was then modified to obtain CaNP@cAD-PEG (Fig. 4A). According to the result of TEM (Fig.4B), compared with the hollow structure of CaNP, a sharp contrast rise was observed in CaNP@cAD-PEG, and the particle size was \sim 180 nm in diameter, a little larger than that of CaNP (\sim 150 nm, Fig. 1A and Supplementary Fig.5B). The successful preparation of CaNP@cAD-PEG was also confirmed by the dynamic change of surface charge during preparation process and the result of element co-localization by Mapping (Fig. 4C, D). The site-specific release of cAD from CaNP@cAD-PEG in TME is critical for simultaneously regulating the phenotype and function of TAMs and reducing the expression of PD-L1 in tumor cells. As part of the design, CaNP with ultra-high pH sensitivity was used as the calcium core, therefore, CaNP@cAD-PEG could achieve efficient superficial disintegration at pH 6.5 within 3 h. Compared with pH 7.4, the morphology of CaNP@cAD-PEG significantly changed, and seem likely returned to CaNP (Fig. 4B), indicating the release of cAD. The release rate was calculated to 75%, which is as high as pH 5.0 (Fig. 4E). In addition, the release of Ca^{2+} at pH 6.5 was also much lower than that at pH 5.0, further confirming the superficial disintegration of CaNP@cAD-PEG. At pH 5.0, more than 85% of total Ca^{2+} was released from CaNP@cAD-PEG (Fig.4F), which provides plenty of Ca^{2+} for regulating the phenotype of TAMs and initiating the shearing effect of cAD (Fig.4G). Interestingly, a significant charge reversal effect of CaNP@cAD-PEG was found after incubating at pH 6.5 for 3 h, from -14.1 mV to 16.3 mV (Supplementary Fig.5C), which is also benefit to the rapid phagocytosis by the main cells (TAMs and tumor cells) in tumor tissue, and play the role of calcium interference.

Motivated by these results, we moved on to explore the feasibility in B16 tumor-bearing mice. Firstly, the biodistribution of CaNP@cAD-PEG was investigated. After 12 hours of tail vein injection, main tissues (heart, liver, spleen, lung, kidney, tumor) were harvested for inductively coupled plasma mass spectrometry (ICP-MS) of Ca^{2+} . The result stated the tumor accumulation characteristics of CaNP@cAD-PEG (Supplementary Fig. 6A), likely due to the enhanced permeability and retention (EPR) effect of tumor. Then, in vivo antitumor efficiency was evaluated according to the schematic diagram (Fig. 4H). The tumor volume and body weight of the mice with different treatments were recorded during the period (Fig. 4K, L and Supplementary Fig. 6B). Compared with the rapid increase of tumor in saline group, there was significant antitumor activity in the CaNP group (tumor inhibition rate: 35%), indicating the stimulating antitumor immune response induced by Ca^{2+} interference. Importantly, the group treated with CaNP@cAD-PEG exhibited the remarkable highest tumor growth inhibition effect (tumor inhibition rate: 82%) than other groups (Fig. 4K, L). Tumor images of different groups further demonstrated that CaNP@cAD-PEG group presented the best antitumor efficacy (Fig. 4I and Supplementary Fig. 6C). Without abnormalities in blood biochemical indexes (The relevant results and description are shown in

Supplementary Fig. 6D), CaNP@cAD-PEG significantly extended the survival rate of mice to 85%. In contrast, none of the saline group survived on day 30 (Fig. 4J). Furthermore, pathological analysis revealed that CaNP@cAD-PEG treatment resulted in a large amount of apoptosis/necrosis as well as a significant reduction of PD-L1 in tumor (Fig. 4M, N and Supplementary Fig. 6E) without damaging to normal organs (Supplementary Fig. 6E). Importantly, the cardiotoxicity induced by PD-L1 antibody was significantly decreased via an alternative Ca²⁺-activating PD-L1 depleting strategy (Supplementary Fig. 6F).

CaNP@cAD-PEG stimulates potent antitumor immunity

Next, we investigated the mechanism of anti-tumor immune efficiency. Considering the TAM phenotypic transformation induced by Ca²⁺ interference in vitro, the phenotype of TAMs in tumor was firstly detected. The proportion of M1-like TAMs was increased after CaNP@cAD-PEG treatment, together with a decreased polarization of M2-like TAMs (Fig. 5A and Supplementary Fig.7A). As the major tumor-infiltrating immune cell population (over 50% of the cells in tumor), the polarization behavior of TAMs will lead to the activation of tumor immunosuppressive microenvironment. For examples, the absolute number of CD103⁺ dendritic cell (DC) was increased, with the decrease of myeloid-derived suppressor cells (MDSCs) and regulatory T cells (Treg) (Fig. 5B, see Supplementary Fig.7B for representative flow cytometric analysis images). Secretion of cytokines including IFN- γ and tumor necrosis factor α (TNF- α) further confirmed the immune responses induced by CaNP@cAD-PEG (Supplementary Fig.7C).

Furthermore, CD8⁺ T cells was significantly increased in CaNP@cAD-PEG treatment as compared to other controls (Fig. 5C and Supplementary Fig.7D). In addition, immunofluorescence staining visually indicated the marked increase in M1 macrophages (Supplementary Fig.8A up), natural killer cell (NK, Supplementary Fig. 8A down) and CD8⁺ T cells in the tumors after CaNP@cAD-PEG treatment (Fig. 5D). The remarkable increase of NK benefits from the innate immune response activated by Ca²⁺ interference. The significant immune response after CaNP@cAD-PEG treatment was also confirmed by the enlarge of lymph nodes (Supplementary Fig. 8B) and DCs, CD8⁺ and CD4⁺ T cell infiltrating in lymph nodes (Supplementary Fig. 8C). Altogether, those results confirmed the effective activation of innate and adaptive immune responses after CaNP@cAD-PEG treatment.

Inspired by the memory-like property of CD8⁺ T lymphocytes, the immune memory response against tumor relapse was investigated via a distal tumor model (Fig. 5E). According to the tumor growth curve, tumor tissue images and TUNEL straining, CaNP@cAD-PEG treatment could significantly inhibit the growth of distal tumors (Fig. 5F, G and Supplementary Fig.9A, B) without abnormalities in body weight (Supplementary Fig. 9C). Furthermore, the effector memory T (T_{EM}) cells in spleen were much higher in CaNP@cAD-PEG group than that in other control groups (Fig. 5H and Supplementary Fig.9D), indicating that CaNP@cAD-PEG treatment induced effectively immune memory effect. To further evaluated the systemic effect of the immune response, a mouse lung metastasis model was performance (Fig. 5I). According to the results in Fig. 5J, CaNP@cAD-PEG treatment displayed much cleaner and smoother lungs in comparison with other groups, significantly suppressing 90% of lung metastasis. These results

implied the potential of CaNP@cAD-PEG for long-term antitumor relapse capability and metastasis prevention.

Discussion

The efficacy of antitumor immunotherapy is often limited by the highly tumor immunosuppressive microenvironment (TME). TAMs are believed as the dominant driver that contribute to the immunosuppressive TME via producing immunosuppressive cytokines, suppressing cytotoxic T cell activity while promoting regulatory T cells, and inhibiting B cell signaling^{32, 33}. Multiple drugs have been exploited to achieve TAM polarization, such as regorafenib, zoledronic acid and miR-155. Despite early preclinical studies and ongoing clinical trials of the conventional small-molecule drugs or nucleic acid drugs, developing new therapeutics with efficient M2→M1 phenotypic conversion, adequate ability to ingested by TAMs in vivo, as well as resulting optimal therapeutic efficacy are still needed^{34, 35}. Metal ions are essential fundamental of all forms of life which nearly half of all enzymes required for their function and are critically involved in virtually all biological processes. Particularly, increasing evidence has mounted to suggest that metal ions are critically implicated in regulating both the innate and adaptive immune response^{9, 24, 36}. In this study, nanoscale calcium successfully led to the burst increase of cytosolic Ca²⁺ in TAMs/tumor cells via bypassing the ion channels. “Ca²⁺ interference” in TAMs showed the dephosphorylation of p38, activation of NF-κB, promoting nuclear localization, thus leading to an efficient M2→M1 phenotypic conversion(23). Furthermore, “Ca²⁺ interference” also promoted the release of NLRP3 inflammasomes, synergetic leading to activation of both innate and acquired immune responses^{37, 38}. Besides TAMs, “Ca²⁺ interference” in tumor cells showed the activation of calmodulin and served as an inducer to the exposure of CRT and the release of HMGB1 for further promoting tumor cell immunogenicity³⁹. Owing to the super pH-sensitivity of calcium nanoparticles, the hydrophilic shell (SDS-PEG2000) on the surface showed improved stability in blood circulation and led to the enhanced tumor accumulation of NPs, while site-specific separating in TME, exposed the electropositive calcium core, which is benefit for the enhanced endocytosis by TAM/tumor cells.

Besides the immunosuppressive tumor microenvironment, another major challenge faced by tumor immunotherapy is the fact that the programmed-death/programmed-death ligand 1 (PD-1/PD-L1) system^{40, 41}. Furthermore, activation of adaptive immune response often leads to the upregulation of PD-L1 in tumors. Antibodies against PD-L1 have shown a great deal of clinical activity in various cancer types^{42, 43}. However, PD-L1 inhibitors are widely distributed in normal cells and often cause adverse autoreactive immune responses and associated side effects^{44, 45}. Hence developing a precise PD-L1 inhibition strategy for tumor cells is still in great demand⁴⁶. In this study, to achieve targeted gene silencing in tumor cells, a circular aptamer-DNAzyme conjugate (cAD) were designed⁴⁷. Firstly, DNAzyme are catalytic nucleic acids that can mimic the function of endonucleases for cleavage of specific mRNA with multiple turnovers, which may be more effective for PD-L1 gene silencing on a per molecule basis. Secondly, cAD had a specific tumor cell targeting ability via splicing a tumor targeting aptamer (sgc8), which guaranteed the specificity of PD-L1 depletion in tumor cells; Thirdly, the closed loop “dumbbell”

structure of cAD brought extremely stability to the DNAzyme, even under the action of nuclease, cAD also displayed an equivalent catalytic activity, thus leading to the higher efficient gene silencing efficiency. More importantly, DNAzymes always need sufficient ion cofactor supply for activation, which just can be solved by our “Ca²⁺ interference” strategy. Since Ca²⁺ release was also specific in tumor site in response to the relatively low pH, this integrated CaNP@cAD-PEG showed high tumor specificity for local PD-L1 suppression. The catalytic shear activity of cAD was specifically activated by Ca²⁺ interference, which in turn reduces potential autoimmune disorders of PD-L1 antibody.

In summary, the rational combination of “Ca²⁺ interference” and targeted depleting checkpoint PD-L1 using Ca²⁺-activating DNAzyme yielded improved efficacy in primary and metastatic tumors without obvious side effects. This previously unknown combination provided an alternative strategy for boosting tumor immunotherapy. In addition, this study serves as a proof of concept for Ca²⁺ induced immunotherapy, which can be easily tailored to other transition metal ions, such as Mn²⁺, Zn²⁺ and Ni²⁺^{12, 48}. Last, this closed loop “dumbbell”-engineering strategy not only improves in vivo stability of DNAzyme, but also can be targeted to various cells types as well as be activated by various metal ions⁴⁹.

Methods

Cell line and cell culture.

B16 mouse melanoma cells obtained from iCell Bioscience Inc. (Shanghai, China) were cultured in RPMI 1640 medium supplemented with 10% fetal bovine serum (FBS) and 1% penicillin-streptomycin solution at 37 °C under 5% Carbon dioxide.

Mice.

4 to 6 weeks-old female C57BL/6 mice (14-18 g) were feed at the condition of 25 °C and 55% of humidity in Experimental Animal Center of Zhengzhou University. All animal studies were performed in accordance with the guidelines approved by Henan laboratory animal center. The license number of C57BL/6 is SCXK (xiang)2019-0004.

Synthesis of CaNP, cAD.

Synthesis of CaO₂ nanoparticle (CaNP): Firstly, 3% hydrogen peroxide solution and 2 mol/L calcium chloride solution were prepared as the original solution. 1 mL of deionized water and 1 ml of calcium chloride were added to 60 ml of absolute methanol in turn. After stirring vigorously for 10 min, 1 ml of hydrogen peroxide was added. After stirring for 5 min, ammonia was added to the mixing system drop by drop until the color changed to Cambridge blue. Centrifugation at 8000 g for 20 min, repeated washing with methanol twice, and finally dispersed in deionized water.

Synthesis of circular aptamer-DNAzyme conjugate (cAD): 8 μL of EtNa (10 μM) and Sgc8 (10 μM) were added to 18 μL of DNase/Rnase-Free water, and then 10 × T4 DNA Ligase Buffer was added. After

incubation at 95 °C for 5 min, the T4 DNA Ligase was rapidly cooled to 16 °C, and then added 2 µL of T4 DNA Ligase. After incubation at 16 °C for 12 hours, the above mixture was heated at 75 °C for another 5 min to obtain cAD.

Investigate the best feeding ratio of CaNP and cAD.

CaNP (5 mg/mL) and cAD (10 µM) were mixed by volume ratio of 1:1, 1:5, 1:10, 1:15, after incubating at room temperature for 4 hours, and 3% agarose gel was prepared to investigate the best feeding ratio of CaNP and cAD. CaNP and cAD were used as the control.

Synthesis of CaNP@cAD-PEG.

CaNP@cAD-PEG was prepared by mixing cAD and CaNP in a volume ratio of 1:10. After incubation for 6 h at room temperature at 300 rpm/min, DSPE-PEG2000 was added in a mass ratio of 2:1 with CaNP. The mixture was shaken at room temperature for another 3 hours and then centrifuged at 8000 g for 20 min to obtain CaNP@cAD-PEG.

Characterization of Sgc8 aptamer targeting efficiency.

Sgc8 and random base sequences were labeled with FAM fluorescence, and 1 µM of Sgc8 and random sequences were incubated with B16 cells at 37 °C for 2 h, respectively. Meanwhile, Sgc8 was co-incubated with HL-7702 cells as the control group, and the fluorescence intensity of each group was detected by a flow cytometer (BD Accuri®C6, American) and data analysis was performed with FlowJo (Version 10).

Cleavage ability of cAD in vitro.

cAD (100 nM) was incubated with an equal amount of PD-L1 mRNA (100 nM) at 37 °C for 12 h in Tris-HCl buffer (pH = 8.8) containing different concentrations of CaCl₂ (1 mM, 10 mM, 20 mM, 30 mM, 40 mM and 50mM), respectively. After incubation, the cleavage efficiency was verified by polyacrylamide gel electrophoresis.

Study on the stability of cAD in vitro.

cAD (100 nM) was incubated with were added to 7.75 µL of DNase/Rnase-Free water, and then 10 × Exo I Buffer and 0.25 µL Exo I was added. After incubation at 37 °C for 1 h, 4 µL 6×DNA loading buffer was then added. The samples were then tested with 3% agarose gel. Meanwhile, Sgc8 and EtNa were also treated as control.

Characterization of CaNP, CaNP@cAD-PEG.

The morphology of CaNP and CaNP@cAD-PEG were detected *via* TEM (Tecnai G2 F20). The particle size potential is obtained by dynamic light scattering. 100 µg/mL of CaNP and CaNP@cAD-PEG nanoparticles in water solution were applied onto a 300-mesh carbon-copper grid. The excess solution was removed by

filter paper. Images were recorded by a transmission electron microscope (JEM 1200EX, JEOL, Japan) operated at a voltage of 120 KV. 1 mL 50 µg/mL CaNP and CaNP@cAD-PEG in deionized water were used to measure the corresponding size distribution and zeta potential by a Zeta sizer (Nano ZS-90, Malvern, UK).

Characterization of CaNP@cAD-PEG in acidic environment

Morphology of CaNP@cAD-PEG in different pH values: CaNP@cAD-PEG (100 µg/mL) was fully dispersed into PBS buffer (pH 7.4, pH 6.5, pH 5.0) for 3 h, respectively. Then the above solution was dripped onto the copper network, and after removing the excess water, the morphology of nano particles was observed by a transmission electron microscope (JEM 1200EX, JEOL, Japan).

Ca²⁺ release from CaNP@cAD-PEG in acidic environment : CaNP@cAD-PEG (100 µg/mL) was fully dispersed into PBS buffer (pH 7.4, pH 6.5, pH 5.0) for 0.5 h, 1 h, 2 h, 4 h, 8 h, 12 h, respectively. Subsequently, the above mixtures were centrifuged at 12000 g for 20 min, the supernatant was collected for Ca²⁺ detection by inductively coupled plasma mass spectrometry (ICP-MS: Aglient 7800).

cAD release from CaNP@cAD-PEG in acidic environment: CaNP@cAD-PEG (cAD was labelled with FAM) was dispersed into different PBS buffer (pH 7.4, pH 6.5 and pH 5.0) at a final concentration of 1 mg/mL, and then incubation at 37 °C, 600 rpm under lucifuge environment for 0.5 h, 1 h, 2 h and 3 h, respectively. The fluorescence intensity was measured by a microplate reader (Ex: 488, Em: 525) (Synergy H1, BioTek, America). The release rate of cAD was calculated by ratio of fluorescence intensity to the total amount.

Cleavage ability of CaNP@cAD-PEG in vitro.

50 µg/mL of CaNP@cAD-PEG were incubated in PBS buffer (pH 7.4, pH 6.5 and pH 5.0) at 37 °C for 12 h, respectively. Subsequently, the above mixtures were centrifuged at 12000 g for 20 min, the supernatant was collected to incubate with PD-L1 mRNA (500 nM) at 37 °C for 12 h in Tris-HCl buffer (pH = 6.8), the cleavage efficiency was verified by polyacrylamide gel electrophoresis.

***In vitro* biodistribution of cAD in B16.**

B16 in Confocal petri dish were incubated with cAD (labelled with FAM, 300 nM) for 2, 4 and 6 h. After incubation, cells were stained with Lyso-Tracker Red (75 nM) for 15 min. Then CLSM images were acquired after staining with Hoechst 33342 for 10 mins (TCS SP8, Leica, Germany).

Intracellular free Ca²⁺ detection in B16.

B16 in confocal petri dish were incubated with CaNP (35 µg/mL) for 0, 2 and 4 h, respectively. After incubation, cells were stained with Flou-3AM (1 µM) for 30 min. And then incubated with Hoechst 33342 for 10 min. Lastly, CLSM images were acquired for characterizing the intracellular free Ca²⁺.

Measurement of PD-L1 expression in B16.

qRT-PCR: cells were seeded at 6-well plates at 1×10^5 per well and cultured for 12 h, and then were incubated with different nanoparticles (CaNP, CaNP@cAD-PEG, CaNP@RcAD, cAD) for 12 h, 35 $\mu\text{g}/\text{mL}$ nanoparticles or 300 nM cAD was applied, respectively. After washed with PBS, cells were incubated with fresh complete medium for another 12 h. And then, precipitate of cells was completely collected by trypsin digestion and centrifugation (2000 rpm, 5 min). Then mRNA was isolated with a Trizol Regent kit (Invitrogen). One microgramme of RNA sample was utilized to obtain cDNA. One microliter of cDNA sample and specific primers were used to amplify PD-L1 cDNA according to the manufacturer's parameters (Custom gene qRT-CANPR Quantitation Kit) on a Real-Time CANPR machine.

Western blot analysis: cells were treated according to the above same method. The cells were collected and washed twice with PBS. Cell precipitations were lysed for 1 h at 4 °C. The protein content was measured by Bradford assay. Western blot analysis was conducted using standard method.

Generation of mouse BMDM.

The bone marrow cells were isolated from female C57BL/6 mice femurs and cultured with 20 ng/mL recombinant M-CSF for 6 days. On day 7, naive macrophages (BMDMs) were collected and then stimulated with 20 ng/mL IL-4 (MCE) plus 20ng/mL IL-13(MCE) or 100 ng/mL LPS (MCE) plus 20 ng/mL IFN- γ (MCE) for 24 h to generate the BMDM-M2 or BMDM-M1 macrophages, respectively.

Cytotoxicity assay of BMDM with different concentration of CaNP.

BMDM in 96-well plates was incubated in medium with different concentration of CaNP (1, 10, 20, 50, 100 $\mu\text{g}/\text{mL}$) for 24 h, respectively. And after washing with PBS, BMDM were incubated in medium with 10 μL Cell Counting Kit-8, after 3 h incubation, absorbance in 450 nm was detected. Cell activity (%) = $[A(\text{lactic acid}) - A(\text{blank})] / [A(\text{lactic acid}) - A(\text{blank})] \times 100$

Intracellular free Ca²⁺ detection in BMDM.

BMDM in confocal petri dish were incubated with CaNP (35 $\mu\text{g}/\text{ml}$) for 0, 2 and 4 h, respectively. After incubation, cells were stained with Flou-3AM (1 μM) for 30 min. And then incubated with Hoechst 33342 for 10 min. Lastly, CLSM images were acquired for characterizing the intracellular free Ca²⁺.

Characterization of polarization of macrophages induced by CaNP.

Western blot analysis: M2-BMDM in 6-well plates were treated with CaNP (35 $\mu\text{g}/\text{mL}$)/ H₂O₂ (0.7 μM)/ Cap (70 $\mu\text{g}/\text{mL}$) for 6 h, after washed with PBS, cells were incubated with fresh complete medium for another 42 h. At the same time, M2-BMDM pretreated with CsA (1 μM) for 2 h were treated according to the above method to confirm the effect of Ca²⁺ on macrophages polarization. The cells were collected and washed twice with PBS. Cell precipitations were lysed for 1 h at 4 °C. The protein content was measured by Bradford assay. Western blot analysis was conducted using standard method.

Flow cytometry analysis: M2-BMDM in 6-well plates were treated with CaNP (35 µg/mL)/ H₂O₂ (0.7 µM)/ Cap (70 µg/mL) for 6 h, after washed with PBS, cells were incubated with fresh complete medium for another 42 h. The cells were collected and washed twice with PBS. Cells were incubated with CD206/CD86/CD11b/F4/80 antibody. And then fluorescence was detected by flow cytometry.

Cytokine secretion: M2-BMDM in 24-well plates were treated with CaNP (35 µg/mL)/ H₂O₂ (0.7 µM)/ Cap (70 µg/mL) for 6 h, after washed with PBS, cells were incubated with fresh complete medium for another 42 h, respectively. The cell supernatant of BMDM was collected into new 1.5 ml tubes, centrifuged at 300 g at 4 °C for 10 min to remove the sediment and detect immediately. ELISAs (EK2143/2-96 (Mouse CXCL9/MIG ELISA Kit), EK201B/3-96 (Mouse IL-1β ELISA Kit), EK212/3-96 (Mouse IL-12p70 ELISA Kit) and EK210/3-96 (Mouse IL-10 ELISA Kit) both from MULTISCIENCES (LIANKE) BIOTECH, CO., LTD) were performed according to standard protocols.

Immunofluorescence analysis of NF-κB nuclear transcription: M2-BMDM in 6-well plates were pre-treated with before treating with CaNP + CAT (CaNP: 35 µg/mL; CAT: 10 ug/mL) for 6h, cells were incubated with fresh complete medium for another 42 h. At the same time, M2-BMDM pretreated with were treated CsA (1 µM) for 2 h fluorescence to observe the effect of Ca²⁺ on NF-κB nuclear transcription.

Detection of macrophage phagocytosis: M2-BMDM in 6-well plates were treated with CaNP (35 µg/mL)/ H₂O₂ (0.7 µM)/ Cap (70 µg/mL) for 6 h, after washed with PBS, cells were incubated with fresh complete medium for another 42 h, respectively. Then, B16 cells were labelled with Cell Tracker Deep Red, BMDM were labelled with Cell Tracker Green. After incubation for 2 h, the cells were collected and washed with PBS for twice. And then fluorescence was detected by flow cytometry.

Detection the effect of macrophage polarization on T cell proliferation.

M2-BMDM in 6-well plates were treated with CaNP (35 µg/mL)/ H₂O₂ (0.7 µM)/ Cap (70 µg/mL) for 6 h, after washed with PBS, cells were incubated with fresh complete medium for another 42 h, respectively. Then, CD8⁺ T cell labelled with CFSE were co-incubated with cell supernatant of BMDM. After incubation for 48 h, CD8⁺ T cell were collected and washed with PBS for twice. And then fluorescence was detected by flow cytometry.

Activation of macrophage inflammasome.

M2-BMDM in 6-well plates were incubated with 500 ng/mL LPS for 4.5 h, after washed with PBS, M2-BMDM were treated with CaNP (35 µg/mL)/ H₂O₂ (0.7 µM)/ Cap (70 µg/mL)/ CaNP + CAT (CaNP: 35 µg/mL; CAT: 10 ug/mL) for 6 h, after washed with PBS, cells were incubated with fresh complete medium for another 42 h, respectively. The cell supernatants were collected to detect IL-1β according to ELISA procedure, and Cell precipitations were lysed for 1 h at 4 °C. The protein content was measured by Bradford assay. Western blot analysis was conducted using standard method.

Biodistribution of CaNP in vivo.

Each BALB/c mouse was subcutaneously injected with B16 cells (1×10^7) on the left armpit. The tumor bearing mice were randomly grouped ($n=3$) when the tumor volume reached 200 mm^3 . The mice were then intravenously injected with $100 \mu\text{L}$ of CaNP (10 mg/mL) and saline as control. After 24 h of adimination, mice were then sacrificed for the major organs (heart, liver, spleen, lung and kidney) and tumors. After concentrated hydrochloric acid digestion for 12 h, the deionized water is diluted and filtered to collect the solution for Ca^{2+} detection by ICP-MS (Aglient 7800).

Biosafety evaluation of CaNP@cAD-PEG in vivo.

After treatment for 5 times, 5 mice from saline and CaNP@cAD-PEG groups were sacrificed by taking blood from the abdominal aorta and the obtained blood was used for blood chemistry analysis and blood routine analysis.

In vivo anti-tumor efficiency.

The B16 tumor-bearing mice were divided randomly into four groups: saline, cAD, CaNP, CaNP@cAD-PEG, aPD-L1, aPD-L1+CaNP (5 in each group). The different formulations were administrated through tail vein injection (cAD: $1 \mu\text{M}$, $200 \mu\text{L}$; CaNP: 5 mg/mL , $200 \mu\text{L}$). The treatments were performed 7 times every 2 days. Body weights and tumor sizes were monitored every other day after the corresponding treatments. The tumor volume was calculated by the equation: Tumor volume = $(\text{width}^2 \times \text{length})/2$. Relative tumor volume was the corresponding changes relative to the initial value measured before treatment. All mice were photographed and euthanized at two weeks post injection, and the tumors, lymph nodes and spleens were taken out and photographed. The collected organs and tumors were fixed immediately in 10% paraformaldehyde solution, followed by standard dehydration and paraffin embedding. The embedded tissues were then sectioned into $4 \mu\text{m}$ slices and then subjected to standard H&E and Tunnel staining for histological analysis.

Detection of PD-L1 expression in B16 tumor.

The tumors were harvested 2 days post the final treatments and cut into small pieces to homogenate. After washing twice with PBS, Cell precipitations were lysed for 1 h at 4°C . The protein content was measured by Bradford assay. Western blot analysis was conducted using standard method.

Detection of immune filtration in tumor.

The tumors were harvested 2 days post the final treatments and cut into small pieces randomly selected and weighed $0.04\text{-}1\text{g}$ (0.18 g), added 2.35 mL RPMI1640, $100 \mu\text{L}$ Enzyme D, $10 \mu\text{L}$ Enzyme R, $12.5 \mu\text{L}$ Enzyme A, and incubated at 37°C for 40 min. Then filtered through a $70 \mu\text{m}$ filter, and 5 mL RPMI1640 was added to rinse the undigelled tissue. Wash it with PBS and suspend it again in 100 uL system. The cell suspension was stained with anti-CD11b-FITC, anti-CD80-PE, anti-CD206-PE for macrophage detection and anti-CD3-FITC, anti-CD45-PE/Cy7, anti-CD4-ACANP, anti-CD8 α -PerCP, anti-FoxP3-PE for CD4/CD8/Treg detection. anti-CD3-FITC, anti-CD45-PE/Cy7, anti-CD8 α -PerCP, anti-IFN- γ -APC for IFN- γ

detection. anti-CD45-FITC, anti-CD11b-PE, anti-CD206-PerCp/cy5.5, anti-CD80-PE/cy7, anti-Gr-1-ACANP for M1/M2/MDSC detection. anti-CD45-PE/cy7, anti-CD11cACANP, anti-CD103-PE for DC detection. Flow cytometry acquisition was performed on a Cyan flow cytometer (BD LSR Fortessa) and data analysis was performed with FlowJo (Version 10).

Detection of the immune memory effect of CD8⁺T cells in spleen.

The mice were killed by dislocating executed 10 days post the distal tumor implantation, soaked in 75% ethanol for 10 min, and the limbs of the mice were fixed on the foam plate with the abdomen facing up with a needle. Pinch the abdominal skin with forceps, scissors cut a small mouth, expose the abdominal wall, tear the skin with two forceps in the small mouth, try to expose the abdomen; The abdominal wall was clamped with forceps, the abdominal cavity was cut open, the spleen was removed, and the spleen was removed with an elbow forceps clamp. The removed spleen was placed in PBS and ground with the frosted surface of a sterilized and pre-wetted glass slide; The ground single cell suspension was filtered through a 70 µm cell screen to remove large tissue mass. The centrifuge was centrifuged at 300×g for 5 min in a cryogenic refrigerated centrifuge. Add erythrocyte lysate (3 times volume), gently beat evenly, and lyse for 5-10 min at room temperature; Wash with PBS 7.2 for 2 times, count, resuspend with PBS 7.2 (containing 1 mM EDTA and 2% FBS), adjust the cell density and stained with anti-CD3-FITC, anti-CD8α-PerCP, anti-CD44-APC and anti-CD62L-PE antibodies. Flow cytometry acquisition was performed on a Cyan flow cytometer (BD LSR Fortessa) and data analysis was performed with FlowJo (Version 10).

Analyze of the treatment-induced cytokine secretion in vivo.

The blood samples were agglutinated for 30 min at room temperature. Centrifuged at 1000 g for 10 min. Serum samples were collected for immediate testing. ELISAs (PT512 (Mouse TNF-α ELISA Kit) and P1580 (Mouse IFN-γ ELISA Kit), both from Beyotime) were performed according to standard protocols.

Immunofluorescence and immunohistochemical analysis of tumor tissues.

Frozen tumor sections were stained with immunofluorescence and immunohistochemical staining. The tumor was first placed in 4% paraformaldehyde (PFA) for 24 h at 4 °C, and then transferred to 15% and 30% sucrose solution (w/w) for dehydration. The tumor was implanted in the optimal cutting medium (O.C.T.) and the frozen section was placed in a cryostat microtome. The dye was rinsed with PBS, permeated, and then sealed at room temperature with 5% bovine serum albumin (BSA) for 1 h, followed by staining with different major antibodies: CD4, CD8, CD206, CD80, DAPI overnight at 4 °C, as per manufacturer's instructions. After adding fluorescently labeled secondary antibodies (goat anti-rat IgG and goat anti-rabbit IgG), the slides were analyzed by confocal microscopy.

Statistical analysis

Statistical analysis Statistics were performed using GraphPad Prism 8. Differences between two experimental groups were determined by two-tailed Student's t test and multiple groups by one-way

ANOVA with Tukey's post-test. Survival curves were assessed with a log-rank (Mantel-Cox) test. TCGA gene data correlations were tested using nonparametric Spearman's test. All bar graphs show means \pm SEM. *P < 0.05, **P < 0.01, ***P < 0.001.

Data availability

The authors declare that all the data supporting the findings of this study are available within the article and its Supplementary Information files, and from the corresponding author on reasonable request.

Declarations

Acknowledgments: The work was supported by the National Natural Science Foundation of China [Nos. 81874304, 82093075, 31900991, U2004197, 21904119]; Innovation Talent Support Program of Henan Province [Nos. 19HASTIT006, 21HASTIT043]; Postdoctoral Science Foundation of China [Nos. BX20200309, 2020M254785]. Authors thank Modern Analysis and Computing Center of Zhengzhou University for technical assistance.

Conflict of interest

The authors declare that they have no conflict of interest.

References

1. D. N. Khalil, E. L. Smith, R. J. Brentjens, J. D. Wolchok, The future of cancer treatment: immunomodulation, CARs and combination immunotherapy. *Nat. Rev. Clin. Oncol.* **13**, 273-290 (2016).
2. J. Galon, D. Bruni, Approaches to treat immune hot, altered and cold tumours with combination immunotherapies. *Nat. Rev. Drug Discov.* **18**, 197-218 (2019).
3. T. F. Gajewski, H. Schreiber, Y.-X. Fu, Innate and adaptive immune cells in the tumor microenvironment. *Nat. Immunol.* **14**, 1014-1022 (2013).
4. H. Phuengkham, L. Ren, I. W. Shin, Y. T. Lim, Nanoengineered Immune Niches for Reprogramming the Immunosuppressive Tumor Microenvironment and Enhancing Cancer Immunotherapy. *Adv. Mater.* **31**, (2019).
5. P. Sharma, S. Hu-Lieskovan, J. A. Wargo, A. Ribas, Primary, Adaptive, and Acquired Resistance to Cancer Immunotherapy. *Cell* **168**, 707-723 (2017).
6. M. A. Branca, Rekindling cancer vaccines. *Nat. Biotechnol.* **34**, 1019-1024 (2016).
7. X. Feng, W. Xu, Z. Li, W. Song, J. Ding, X. Chen, Immunomodulatory Nanosystems. *Adv. Sci.* **6**, (2019).
8. S. Musetti, L. Huang, Nanoparticle-Mediated Remodeling of the Tumor Microenvironment to Enhance Immunotherapy. *ACS Nano* **12**, 11740-11755 (2018).
9. M. Vig, J.-P. Kinet, Calcium signaling in immune cells. *Nat. Immunol.* **10**, 21-27 (2009).

10. R. E. Dolmetsch, R. S. Lewis, C. C. Goodnow, J. I. Healy, Differential activation of transcription factors induced by Ca²⁺ response amplitude and duration. *Nature* **386**, 855-858 (1997).
11. N. Ho, M. Gullberg, T. Chatila, Activation protein 1-dependent transcriptional activation of interleukin 2 gene by Ca²⁺/calmodulin kinase type IV/Gr. *J. Exp. Med.* **184**, 101-112 (1996).
12. M. Trebak, J.-P. Kinet, Calcium signalling in T cells. *Nat. Rev. Immunol.* **19**, 154-169 (2019).
13. A. V. Gourine, V. Kasymov, N. Marina, F. Tang, M. F. Figueiredo, S. Lane, A. G. Teschemacher, K. M. Spyer, K. Deisseroth, S. Kasparov, Astrocytes Control Breathing Through pH-Dependent Release of ATP. *Science (New York, N.Y.)* **329**, 571-575 (2010).
14. D. V. Krysko, A. D. Garg, A. Kaczmarek, O. Krysko, P. Agostinis, P. Vandenabeele, Immunogenic cell death and DAMPs in cancer therapy. *Nat. Rev. Cancer* **12**, 860-875 (2012).
15. S. L. Topalian, J. M. Taube, D. M. Pardoll, Neoadjuvant checkpoint blockade for cancer immunotherapy. *Science* **367**, (2020).
16. J. Condeelis, J. W. Pollard, Macrophages: Obligate Partners for Tumor Cell Migration, Invasion, and Metastasis. *Cell* **124**, 263-266 (2006).
17. J. Wang, H. Wang, H. Wang, S. He, R. Li, Z. Deng, X. Liu, F. Wang, Nonviolent Self-Catabolic DNAzyme Nanosponges for Smart Anticancer Drug Delivery. *ACS Nano* **13**, 5852-5863 (2019).
18. W. Huo, X. Li, B. Wang, H. Zhang, J. Zhang, X. Yang, Y. Jin, Recent advances of DNAzyme-based nanotherapeutic platform in cancer gene therapy. *Biophysics Reports* **6**, 256-265 (2020).
19. S. Fu, L. Q. Sun, DNAzyme-based therapeutics for cancer treatment. *Future med. chem.* **7**, 1701-1707 (2015).
20. R. K. Sigel, A. M. Pyle, Alternative roles for metal ions in enzyme catalysis and the implications for ribozyme chemistry. *Chem. rev.* **107**, 97-113 (2007).
21. Y. Lu, New transition-metal-dependent DNAzymes as efficient endonucleases and as selective metal biosensors. *Chem. (Weinheim an der Bergstrasse, Germany)* **8**, 4589-4596 (2002).
22. J. Shi, P. W. Kantoff, R. Wooster, O. C. Farokhzad, Cancer nanomedicine: progress, challenges and opportunities. *Nat. rev.. Cancer* **17**, 20-37 (2017).
23. D. Chen, J. Xie, R. Fiskesund, W. Dong, X. Liang, J. Lv, X. Jin, J. Liu, S. Mo, T. Zhang, F. Cheng, Y. Zhou, H. Zhang, K. Tang, J. Ma, Y. Liu, B. Huang, Chloroquine modulates antitumor immune response by resetting tumor-associated macrophages toward M1 phenotype. *Nat. Commun.* **9**, (2018).
24. C. Wang, R. Zhang, X. Wei, M. Lv, Z. Jiang, in *Advances in Immunology in China - Part B.* (2020), pp. 187-241.
25. J. Liu, C. Zhu, L. Xu, D. Wang, W. Liu, K. Zhang, Z. Zhang, J. Shi, Nanoenabled Intracellular Calcium Bursting for Safe and Efficient Reversal of Drug Resistance in Tumor Cells. *Nano Letters* **20**, 8102-8111 (2020).
26. M. Zhang, R. Song, Y. Liu, Z. Yi, X. Meng, J. Zhang, Z. Tang, Z. Yao, Y. Liu, X. Liu, W. Bu, Calcium-Overload-Mediated Tumor Therapy by Calcium Peroxide Nanoparticles. *Chem* **5**, 2171-2182 (2019).

27. J. An, K. Zhang, B. Wang, S. Wu, Y. Wang, H. Zhang, Z. Zhang, J. Liu, J. Shi, Nanoenabled Disruption of Multiple Barriers in Antigen Cross-Presentation of Dendritic Cells via Calcium Interference for Enhanced Chemo-Immunotherapy. *ACS Nano* **14**, 7639-7650 (2020).
28. K. Shimada, Timothy R. Crother, J. Karlin, J. Dagvadorj, N. Chiba, S. Chen, V. K. Ramanujan, Andrea J. Wolf, L. Vergnes, David M. Ojcius, A. Rentsendorj, M. Vargas, C. Guerrero, Y. Wang, Katherine A. Fitzgerald, David M. Underhill, T. Town, M. Ardit, Oxidized Mitochondrial DNA Activates the NLRP3 Inflammasome during Apoptosis. *Immunity* **36**, 401-414 (2012).
29. G.-S. Lee, N. Subramanian, A. I. Kim, I. Aksentijevich, R. Goldbach-Mansky, D. B. Sacks, R. N. Germain, D. L. Kastner, J. J. Chae, The calcium-sensing receptor regulates the NLRP3 inflammasome through Ca^{2+} and cAMP. *Nature* **492**, 123-127 (2012).
30. K. Zhang, Y. Li, J. Liu, X. Yang, Y. Xu, J. Shi, W. Liu, J. Li, Y-Shaped Circular Aptamer–DNAzyme Conjugates for Highly Efficient in Vivo Gene Silencing. *CCS Chem.* **2**, 631-641 (2020).
31. T. Yu, W. Zhou, J. Liu, Screening of DNAzyme mutants for highly sensitive and selective detection of calcium in milk. *Analytical Methods* **10**, 1740-1746 (2018).
32. C. Ngambenjawong, H. H. Gustafson, S. H. Pun, Progress in tumor-associated macrophage (TAM)-targeted therapeutics. *Adv. Drug Deliv. Rev.* **114**, 206-221 (2017).
33. Q. Yang, N. Guo, Y. Zhou, J. Chen, Q. Wei, M. Han, The role of tumor-associated macrophages (TAMs) in tumor progression and relevant advance in targeted therapy. *Acta pharm. Sin. B* **10**, 2156-2170 (2020).
34. B. Chatterjee, P. Saha, S. Bose, D. Shukla, N. Chatterjee, S. Kumar, P. P. Tripathi, A. K. Srivastava, MicroRNAs: As Critical Regulators of Tumor- Associated Macrophages. *Int J Mol Sci.* **21**, 7117 (2020).
35. M. L. Squadrito, M. Etzrodt, M. De Palma, M. J. Pittet, MicroRNA-mediated control of macrophages and its implications for cancer. *Trends Immunol.* **34**, 350-359 (2013).
36. S. Feske, Calcium signalling in lymphocyte activation and disease. *Nat. Rev. Immunol.* **7**, 690-702 (2007).
37. K. V. Swanson, M. Deng, J. P. Y. Ting, The NLRP3 inflammasome: molecular activation and regulation to therapeutics. *Nat. Rev. Immunol.* **19**, 477-489 (2019).
38. T. Gong, Y. Yang, T. Jin, W. Jiang, R. Zhou, Orchestration of NLRP3 Inflammasome Activation by Ion Fluxes. *Trends Immunol.* **39**, 393-406 (2018).
39. L. J. Sang, H. Q. Ju, G. P. Liu, T. Tian, G. L. Ma, Y. X. Lu, Z. X. Liu, R. L. Pan, R. H. Li, H. L. Piao, J. R. Marks, L. J. Yang, Q. Yan, W. Wang, J. Shao, Y. Zhou, T. Zhou, A. Lin, LncRNA CamK-A Regulates $Ca(2+)$ -Signaling-Mediated Tumor Microenvironment Remodeling. *Mol Cell* **72**, 71-83.e77 (2018).
40. P. S. Hegde, D. S. Chen, Top 10 Challenges in Cancer Immunotherapy. *Immunity* **52**, 17-35 (2020).
41. M. F. Sanmamed, L. Chen, A Paradigm Shift in Cancer Immunotherapy: From Enhancement to Normalization. *Cell* **175**, 313-326 (2018).

42. X. Shen, B. Zhao, Efficacy of PD-1 or PD-L1 inhibitors and PD-L1 expression status in cancer: meta-analysis. *BMJ* **362**, k3529-k3529 (2018).
43. B. Liu, Y. Song, D. Liu, Recent development in clinical applications of PD-1 and PD-L1 antibodies for cancer immunotherapy. *J Hematol Oncol.* **10**, (2017).
44. L. Leroy, X. Lafarge, L. Blouin, F. Bijou, F. Durrieu, E. Olivier, S. Le Moulec, A fatal allo- and immune-mediated thrombocytopenia with a PD-L1 inhibitor. *Ann Oncol.* **29**, 514-515 (2018).
45. Y. Wang, S. Zhou, F. Yang, X. Qi, X. Wang, X. Guan, C. Shen, N. Duma, J. Vera Aguilera, A. Chintakuntlawar, K. A. Price, J. R. Molina, L. C. Pagliaro, T. R. Halfdanarson, A. Grothey, S. N. Markovic, G. S. Nowakowski, S. M. Ansell, M. L. Wang, Treatment-Related Adverse Events of PD-1 and PD-L1 Inhibitors in Clinical Trials. *JAMA Oncol.* **5**, (2019).
46. M. Yi, D. Jiao, H. Xu, Q. Liu, W. Zhao, X. Han, K. Wu, Biomarkers for predicting efficacy of PD-1/PD-L1 inhibitors. *Mol. Cancer* **17**, (2018).
47. H. Fan, Z. Zhao, G. Yan, X. Zhang, C. Yang, H. Meng, Z. Chen, H. Liu, W. Tan, A Smart DNAzyme-MnO₂ Nanosystem for Efficient Gene Silencing. *Angew Chem Int Ed Engl.* **54**, 4801-4805 (2015).
48. M. Vaeth, J. Yang, M. Yamashita, I. Zee, M. Eckstein, C. Knosp, U. Kaufmann, P. Karoly Jani, R. S. Lacruz, V. Flockerzi, I. Kacs Kovics, M. Prakriya, S. Feske, ORAI2 modulates store-operated calcium entry and T cell-mediated immunity. *Nat. Commun.* **8**, (2017).
49. B. Chaigne-Delalande, M. J. Lenardo, Divalent cation signaling in immune cells. *Trends Immunol.* **35**, 332-344 (2014).

Figures

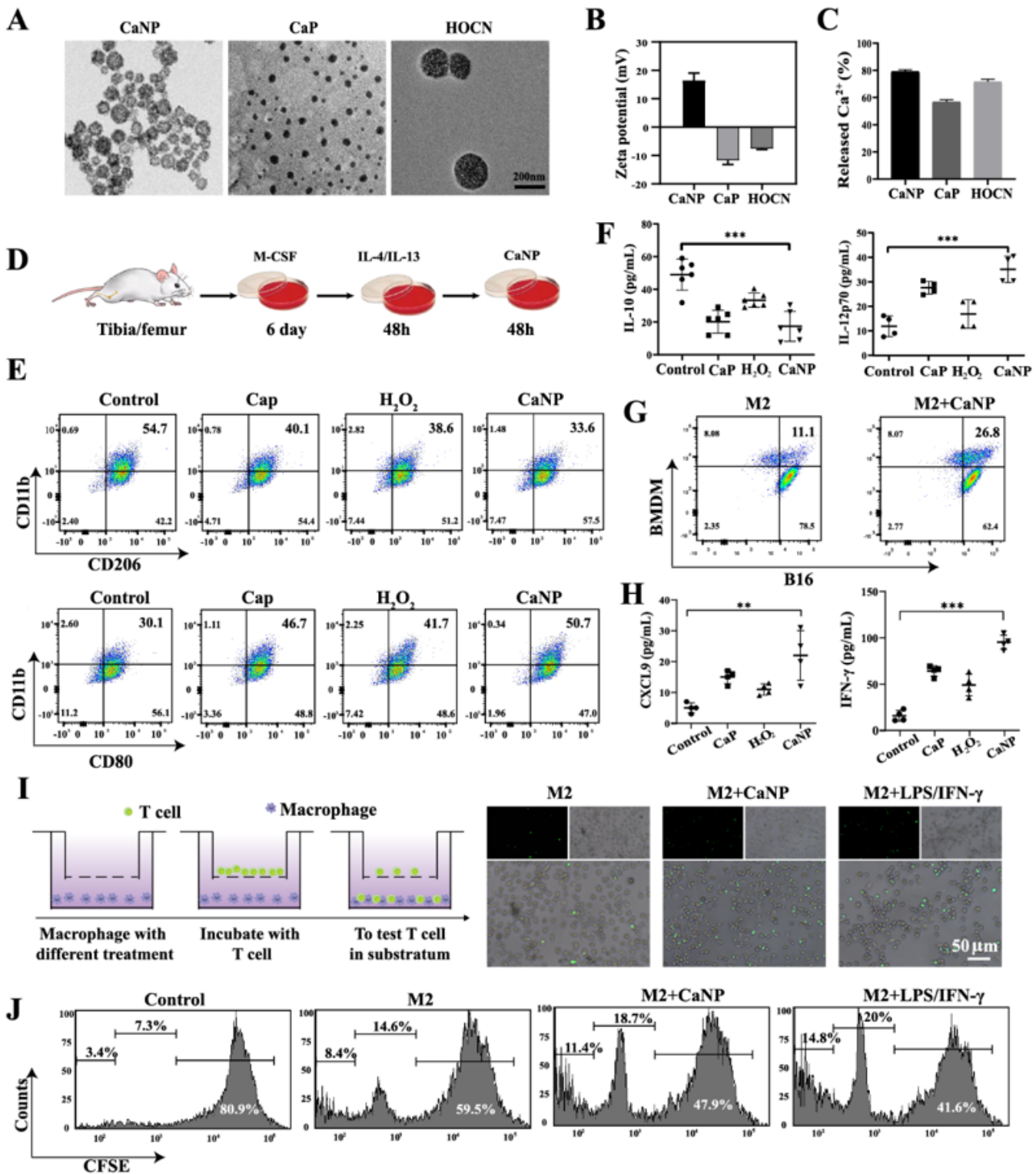


Figure 1

CaNP resets BMDM-M2 to M1 phenotype. (A) Transmission electron microscopy (TEM) image of CaNP, Cap, HOCN at pH 7.4. Scale bar, 200 nm. (B) Zeta potential of CaNP, Cap, HOCN by dynamic light scattering (n=4). (C) Percentage of Ca²⁺ release from CaNP, Cap, HOCN after incubating at pH 5.0 of PBS for 12 h at 37 °C (n=4). (D) Schematic diagram of extraction and treatment of BMDM. (E) Representative flow cytometric analysis images of M2 macrophages (CD206+) and M1 macrophages (CD80+). (F) IL-10

and IL-12p70 levels in cell culture supernatant of different treatment (n=4). (G) Representative flow cytometric analysis images of the phagocytosis of B16 cells by BMDMs before and after CaNP treatment. (H) CXCL9 and IFN- γ levels in cell culture supernatant of different treatment (n=4). (I) Schematic diagram of BMDM recruitment of T cells (left) and representative images (right). Scale bar, 50 μ m. (J) Representative flow cytometric analysis of T cell proliferation with cell culture supernatant from different treatments of BMDM. Data shown are representative of four independent experiments and error bars represent mean \pm SEM. *P < 0.05; **P < 0.01; ***P < 0.001 (Student's t-test)

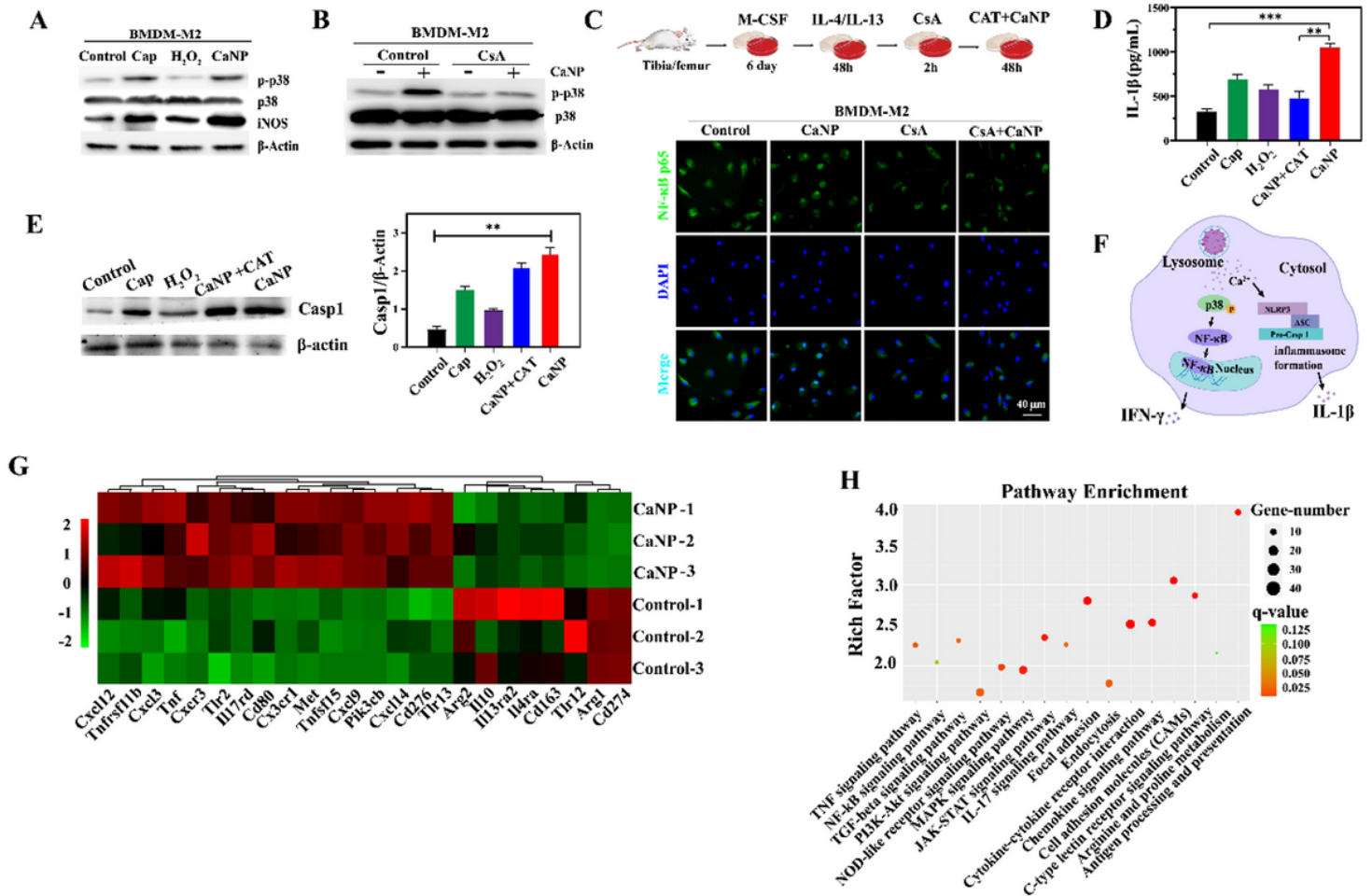


Figure 2

CaNP resets BMDM-M2 through multiple mechanisms. (A) Western blotting of iNOS, total p38, p-p38, and β -actin in H₂O₂, CaNP and Cap treated BMDM-M2 cells for 48 h. (B) Western blotting of total p38, p-p38 and β -actin in BMDM-M2 cells treated with CaNP or PBS after pretreated with 1 μ M CsA or not for 2 h. (C) Schematic diagram (up) and representative CLSM image of the distribution of NF- κ Bp65 (down) in BMDM-M2 cells pretreated with 1 μ M CsA or not for 2 h before addition of CaNP or PBS. Blue, DAPI, green, NF- κ Bp65. Scale bar, 40 μ m. (D) IL-1 β levels in BMDM-M2 cells supernatant after treatment with H₂O₂, Cap, CaNP, CaNP+CAT for 48 h (CAT: 10 μ g/mL) (n=4). (E) Western blotting (left) and the corresponding quantification of Casp 1 in BMDM-M2 cells after treatment with H₂O₂, Cap, CaNP, CaNP+CAT for 48 h (CAT: 10 μ g/mL). (F) Schematic showing CaNP polarized BMDM-M2 through multiple mechanisms. (G) Transcriptome analysis of BMDM-M2 after treated with CaNP or PBS for 48 h.

Differential gene cluster analysis is shown as a heat map. (H) KEGG pathway enrichment analysis of differentially expressed genes between CaNP and PBS treatment group. Data shown are representative of four independent experiments and error bars represent mean \pm SEM. * $P < 0.05$; ** $P < 0.01$; *** $P < 0.001$ (Student's t-test)

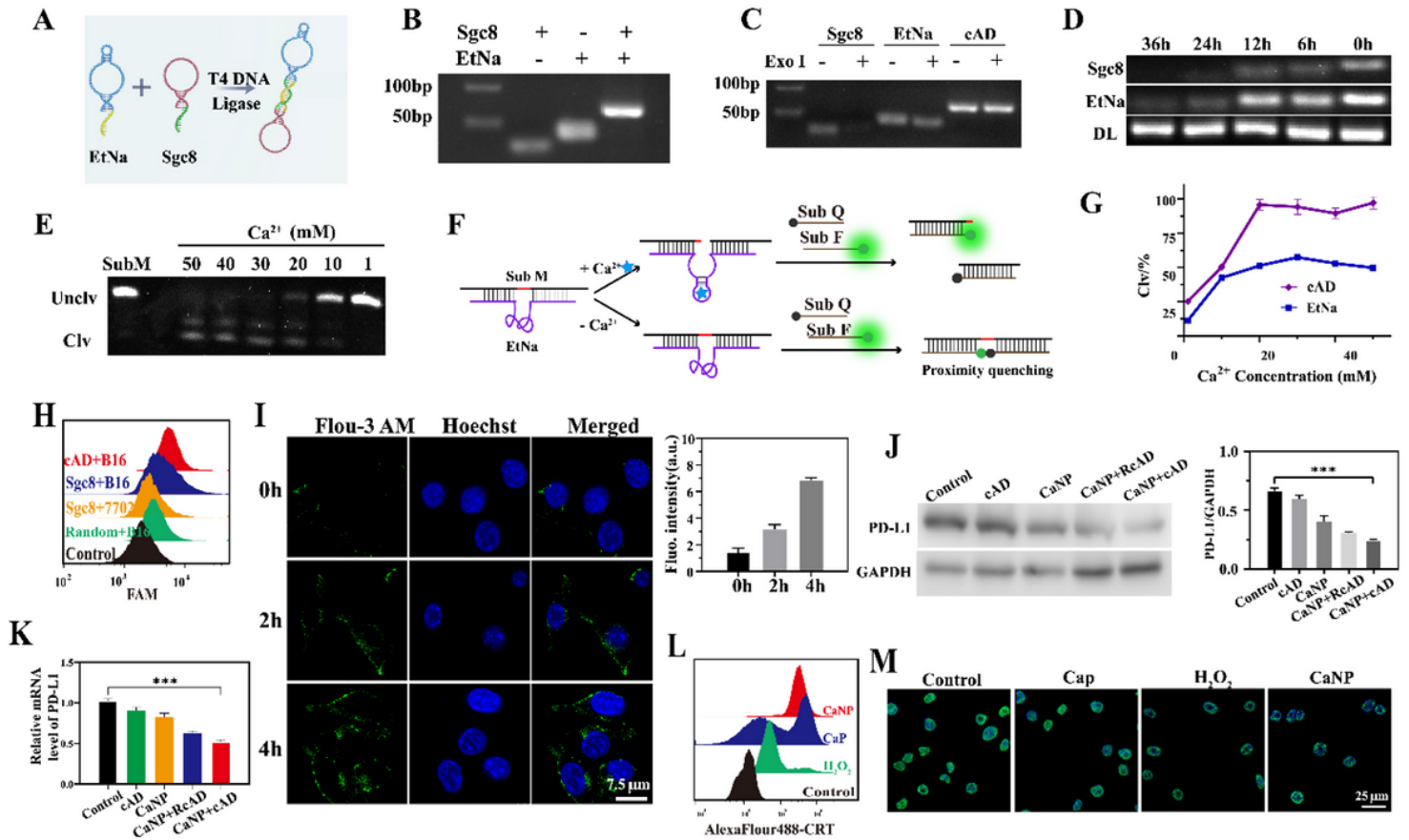


Figure 3

Ca²⁺ activated cAD with specific tumor-targeting and enhanced stabilities efficiently depletes PD-L1 in tumor cells. (A) The design, composite and preparation of cAD. (B) The 3% agarose gel demonstrated the successful synthesis of cAD. (C) After incubation with or without 0.25 U/ μ L Exo I for 1 h, the stability of Sgc8, EtNa and cAD was detected by 3% agarose gel electrophoresis. (D) 3% agarose gel electrophoresis analysis of Sgc8, EtNa and cAD stability after incubation with 10% FBS for different times. (E) The cleavage ability of cAD in different concentrations of Ca²⁺ determined by denaturing PAGE gel. (F) Schematic diagram of CAD shear activity detected by fluorescence. (G) Analysis of the cleavage kinetics of EtNa and cAD (n=4). (H) Representative flow cytometric analysis images of tumor-targeting of cAD. Random denotes for the target sequence of Sgc8 was all changed to Thymine (See Supplementary table 1 for specific sequence information). (I) Representative CLSM image (left) and the corresponding fluorescence quantification (right) of Ca²⁺ levels in B16 cells. Green, Flou-3 AM; blue, DAPI. Scale bar: 7.5 μ m. (J) The expression (left) and the corresponding fluorescence quantification (right) of PD-L1 and GAPDH in B16 cells after treatment with cAD, CaNP, CaNP+ RcAD and CaNP+cAD. RcAD denotes for the shear sequence of EtNa was all changed to Thymine (See Supplementary table 2 for specific sequence information).

information). (K) qPCR analysis of the expression of PD-L1 mRNA in B16 cells after treatment with cAD, CaNP, CaNP+RcAD and CaNP+cAD (n=4). (L) Representative flow cytometric analysis of the exposure of CRT in B16 cells after treatment with H₂O₂, Cap and CaNP. M) Representative CLSM image of HMGB1 released from the nucleus of B16 cells. Green, HMGB1; blue, DAPI. Scale bar: 25 μ m. Data shown are representative of four independent experiments and error bars represent mean \pm SEM. *P < 0.05; **P < 0.01; ***P < 0.001 (Student's t-test)

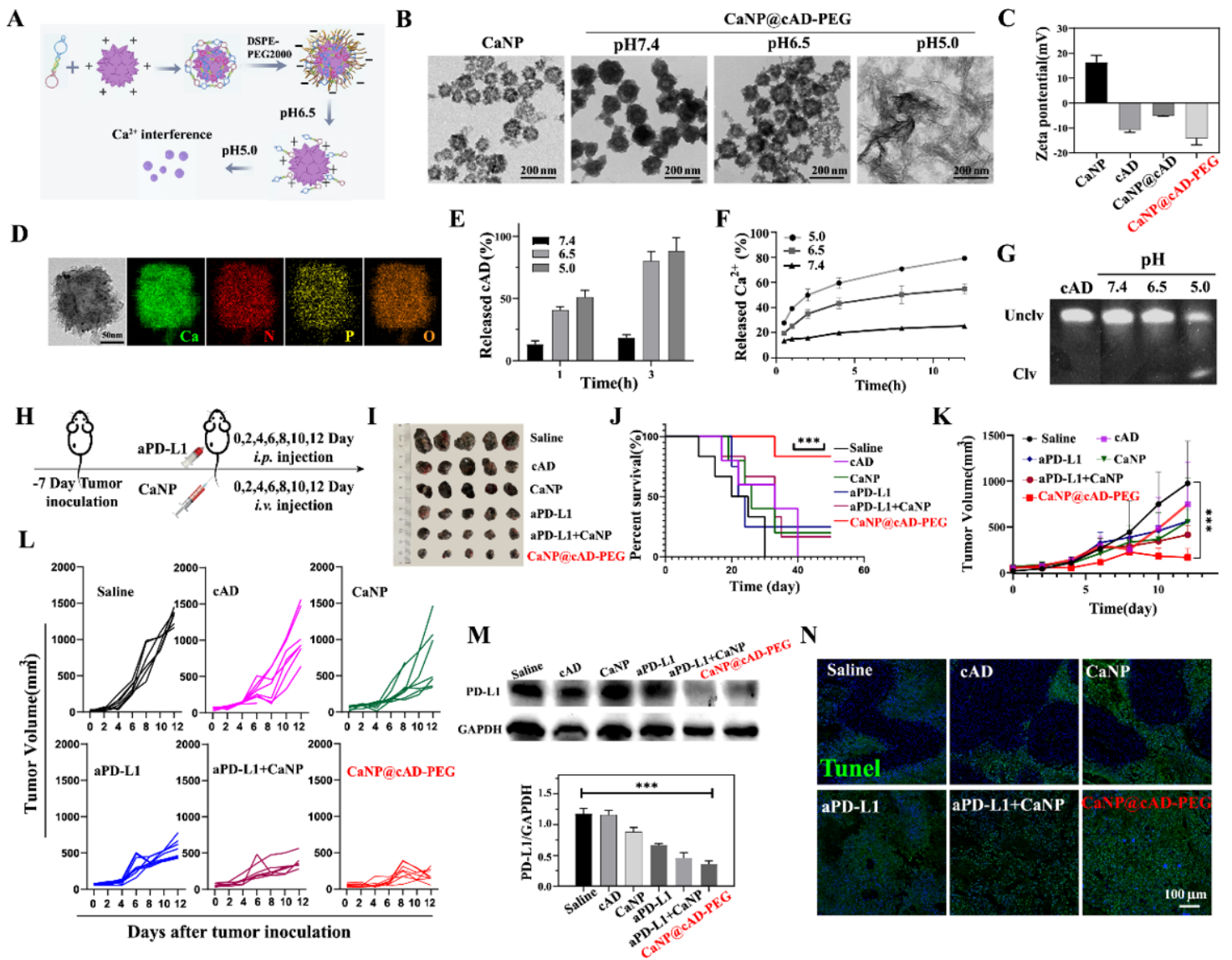


Figure 4

CaNP@cAD-PEG effectively inhibited tumor growth. (A) Schematic depiction of the synthesis process of CaNP@cAD-PEG; (B) The TEM image of CaNP and CaNP@cAD-PEG in different pH values of PBS for 3 h. Scale bar: 200 nm. (C) Zeta potential of CaNP, cAD, CaNP@cAD, CaNP@cAD-PEG by dynamic light scattering (n=3). (D) Elemental mapping analysis of Ca (green), N (red), P (yellow) and O (orange), scale bar: 50 nm. (E) Release profiles of cAD from CaNP@cAD-PEG after incubated in pH 7.4, pH 6.5 and pH 5.0 for 1h and 3h, respectively (n=3). (F) Release of Ca²⁺ from CaNP@cAD-PEG after incubation in pH 7.4, pH 6.5 and pH 5.0 for 12h, respectively (n=3). (G) The cleavage ability of CaNP@cAD-PEG after

incubation in different pH values determined by denaturing PAGE gel. (H) The therapeutic design of primary tumor model. (I) Representative images of tumor tissues in different treatment groups. (J) Survival curves of mice in the different treatment groups in the primary tumor model (n=5). (K) Tumor growth curves of mice in the different treatment groups in the primary tumor model (n=5). (L) Individual tumor growth curves of mice in the different treatment groups in the primary tumor model (n=5). (M) SDS-PAGE protein analysis (up) and Gray value semi-quantitative (down) of the expression of PD-L1 in the tumor of different group (n=3). (N) Representative TUNEL images of tumor in different groups. Scale bars, 100 μ m. Data are represented as means \pm SEM. * P < 0.05, ** P < 0.01, and *** P < 0.001 (one-way ANOVA with Bonferroni post hoc test and Student's t test).

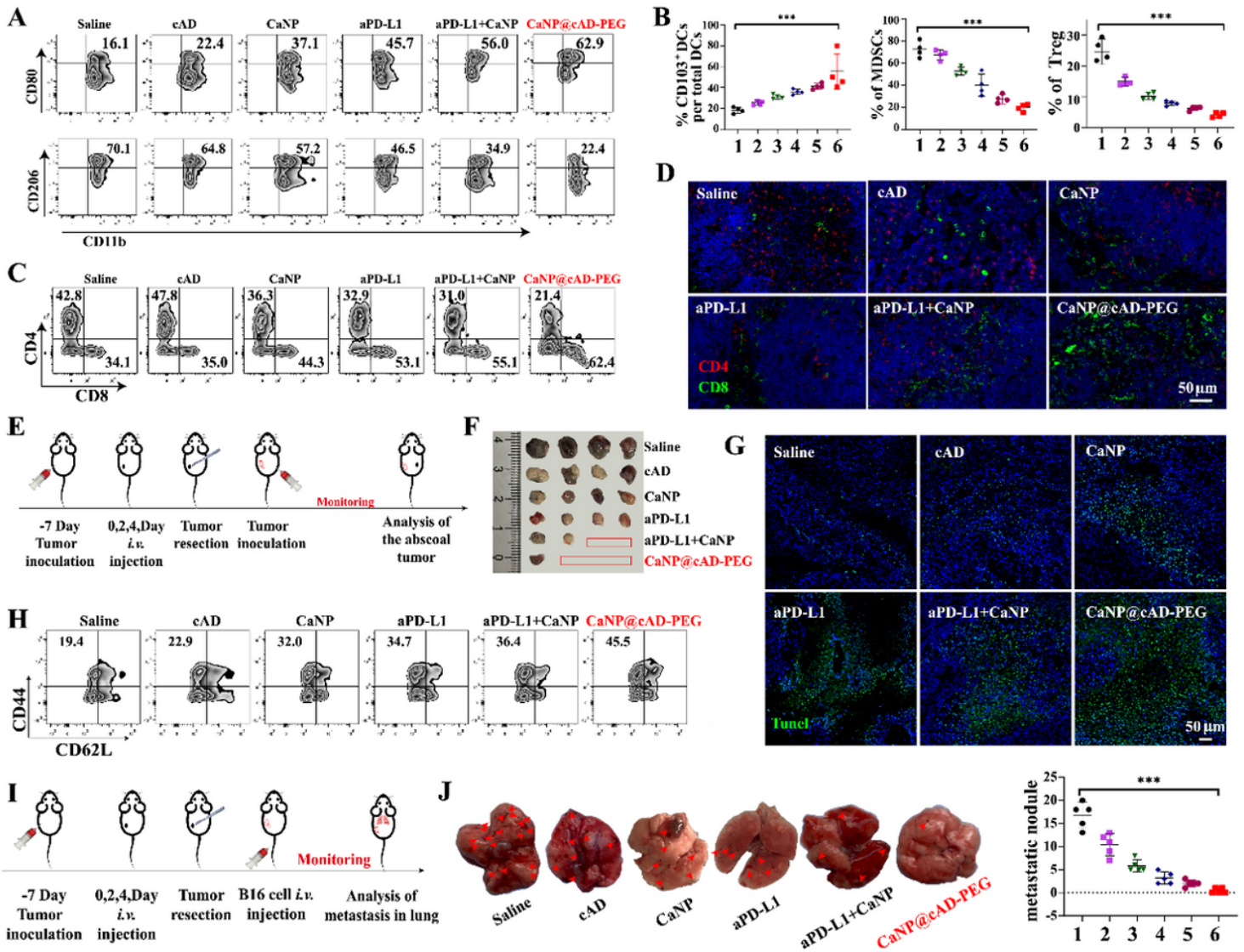


Figure 5

CaNP@cAD-PEG effectively activates systemic antitumor immune response. 1: Saline; 2: cAD; 3: CaNP; 4: aPD-L1; 5: aPD-L1+CaNP; 6: CaNP@cAD-PEG. (A) Representative flow cytometric analysis images of M1-macrophage (CD80hi) and M2-macrophage (CD206hi, gate on CD45+CD11b+) cell infiltrated in tumor. (B) The relative quantification of DCs (CD103hi, gate on CD45+CD11c+), MDSC (Gr-1hi, gate on

CD45+CD11b+) and Treg (FOXP3hi, gate on CD45+CD3+ CD4+) infiltrated in tumor (n=5). (C) Representative flow cytometric analysis images of CD4+/CD8+ T cell (gate on CD45+CD3+) infiltrated in tumor (n=5). (D) Representative immunofluorescence images of tumors showing CD4+ (red), CD8+ (green) T cell infiltration in tumor of different groups. Scale bars, 50 μ m. (E) The therapeutic design of abscopal tumor model. (F) Images of abscopal tumor in different groups. (G) Representative TUNEL images of tumor in different groups. Scale bars, 50 μ m. (H) Representative flow cytometric analysis images of TEM cell (gate on CD3+CD8+) in spleen. (I) The therapeutic design of lung metastatic tumor model. (J) Representative lung images (left) and relative quantification (right) of metastatic nodules in each treatment group (n=5). The red arrows indicate metastatic nodules. Data are represented as means \pm SEM. *P < 0.05, **P < 0.01, and ***P < 0.001 (one-way ANOVA with Bonferroni post hoc test and Student's t test).

Supplementary Files

This is a list of supplementary files associated with this preprint. Click to download.

- [supplementarymaterialstonaturecommunication.docx](#)
- [Scheme1.png](#)